Xi Feng; Xueqian Zhang ✉ 🄳 ; Haidi Qiu; Quan Xu 🄳 ; Weili Zhang ✉ 🄳 ; Jiaguang Han ✉ 🄳

View Online

Export Citation

Applied Physics Letters

Nonlinear binary indium-tin-oxide terahertz emitters with complete phase and amplitude control ⓕ

Xi Feng,[1] Xueqian Zhang,[1,a)] ⓘD Haidi Qiu,[1] Quan Xu,[1] ⓘD Weili Zhang,[2,a)] ⓘD and Jiaguang Han[1,3,a)] ⓘD

AFFILIATIONS

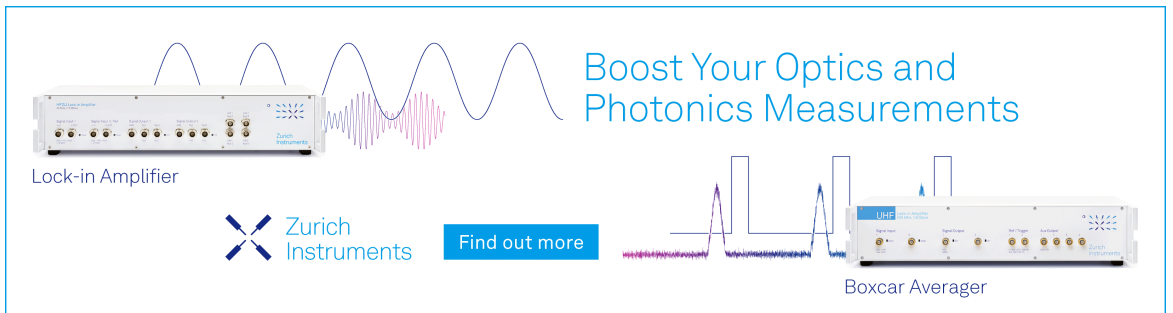[1]Center for Terahertz Waves and College of Precision Instrument and Optoelectronics Engineering, and The Key Laboratory of Optoelectronics Information and Technology (Ministry of Education), Tianjin University, Tianjin 300072, China
[2]School of Electrical and Computer Engineering, Oklahoma State University, Stillwater, Oklahoma 74078, USA
[3]Guangxi Key Laboratory of Optoelectronic Information Processing, School of Optoelectronic Engineering, Guilin University of Electronic Technology, Guilin 541004, China

[a)]Authors to whom correspondence should be addressed: alearn1988@tju.edu.cn; weili.zhang@okstate.edu; and jiaghan@tju.edu.cn

ABSTRACT

Terahertz (THz) waves have demonstrated immense potential for various applications in multiple fields. To enable the development of compact THz applications, it is crucial to integrate THz emission and wavefront manipulation into a single device. This study proposes and experiments with a nonlinear binary THz emitter that utilizes a patterned indium-tin-oxide (ITO) film. By precisely controlling the displacements and area sizes of the composed ITO patches, we are able to fully and independently manipulate the phase and amplitude of the locally emitted THz wave at the +1st-order diffraction, so as to the corresponding wavefront. Our innovative approach provides a promising path toward miniaturized and functioning THz devices and systems.

Published under an exclusive license by AIP Publishing. https://doi.org/10.1063/5.0198641

Over the past two decades, there has been widespread interest in terahertz (THz) waves due to their potential in various applications, such as high-speed wireless communications,[1] nondestructive sensing,[2,3] and security imaging.[4] Among these applications, the manipulation of THz wavefronts to meet specific requirements stands as a critically important process, which enables THz waves to acquire additional optical properties, greatly expanding the boundaries of THz technologies. For example, THz beams with simple focusing or diverging wavefronts are extensively applied in THz beam shaping and imaging.[5] THz vortex beam can substantially enhance wireless communication capacity by offering infinite multiplexing channels corresponding to an unlimited number of orbital angular momenta (OAM) eigenstates.[6]

So far, there have been significant advancements in methods for manipulating THz wavefronts.[7,8] One common approach involves using conventional optical elements, such as lenses, spiral phase plates,[9] and Fresnel zone plates.[10] Another approach involves using metasurfaces to achieve versatile THz wavefront manipulations by controlling their local phase and amplitude.[11,12] However, both methods typically require the use of separate devices for THz emission and

manipulation, which poses challenges for future miniaturized applications. To address this issue, researchers have explored the integration of THz emission and wavefront manipulation processes into a single device. Related studies have examined the use of nonlinear crystal pumped by structured laser,[13,14] nonlinear metasurfaces,[15–17] patterned functional films,[18,19] etc. However, the methods of using structured lasers and metasurfaces for THz wavefront manipulation typically rely on complex laser shaping techniques and expensive nanoscale fabrication processes, respectively. While patterned functional films are free from the aforementioned requirements, however, the existing studies can only provide limited phase and amplitude control over the emitted THz wavefront, such as two-level phase control[18] or amplitude control,[19] which is not conducive to versatile applications in modern optics. Since that, there is a significant demand for simpler and cost-effective approaches that can provide full control over both phase and amplitude of the THz emissions, allowing greater degrees of freedom in wavefront manipulation.

In this Letter, we propose a nonlinear binary THz emitter (NBTE) that utilizes ultrathin patch array made of indium-tin-oxide

(ITO) film. Our recent preliminary work has already demonstrated the capability of broadband nonlinear THz emission in ITO film under femtosecond laser pump.[20,21] Owing to the centro-symmetric property of ITO and the in-plane C_∞ symmetry of ITO film, the nonlinear THz emission by the difference frequency generation effect only happens at the ITO interface with the p-polarized pump component. The core of our proposed NBTE here includes straightforward phase control by varying the position offset of the ITO patch, and amplitude control by varying the size of the ITO patch. This can be referred to as binary optics and binary holography derived from diffraction theory.[22] To validate such a control ability, three different functionalities working at the +1st-order diffraction, including focusing, single focusing vortex, and mixed focusing vortex THz emissions, are experimentally demonstrated. Our method offers a promising solution for achieving diverse functional THz emitters.

Figure 1(a) schematically illustrates four basic unit cells of our NBTE composed of rectangular ITO patches, where O is the coordinate origin of the whole NBTE, α is the azimuthal angle of the unit cell, P is the period, ΔP is the center displacement of the ITO patch to the unit cell along the x direction, and $\eta_x P$ and $\eta_y P$ are the lengths of the ITO patch along the x and y directions, respectively. Here, P is larger than the working wavelength λ_{THz} to allow diffraction. As shown in Fig. 1(b), the NBTE is obliquely illuminated by a p-polarized infrared femtosecond pump beam with an incident angle of θ_0, where the THz wave emitted from each ITO patch radiates outside in a wide angle range, and only the THz wave toward the nth-order diffraction with an output angle of θ is manipulated. According to the nonlinear difference frequency generation equation, the initial phase of the emitted THz wave from the ITO patch can be defined by $\varphi_{THz,0} = dk_{THz}$, where d represents the propagation distance of the pump beam and $k_{THz} = 2\pi/\lambda_{THz}$ represents the wave vector of the emitted THz wave.[19] Therefore, for the nth-order diffraction, the THz wavelength also satisfies the classic grating equation of $n\lambda_{THz} = P[\sin(\theta_0) - \sin(\theta)]$. Considering two THz fields $E_{THz,1}$ and $E_{THz,2}$ generated from one ITO patch when it is, respectively, at the unit cell center and at an offset position ΔP, see Fig. 1(b), there will be a phase difference $\Delta\varphi$ between them which can be described by
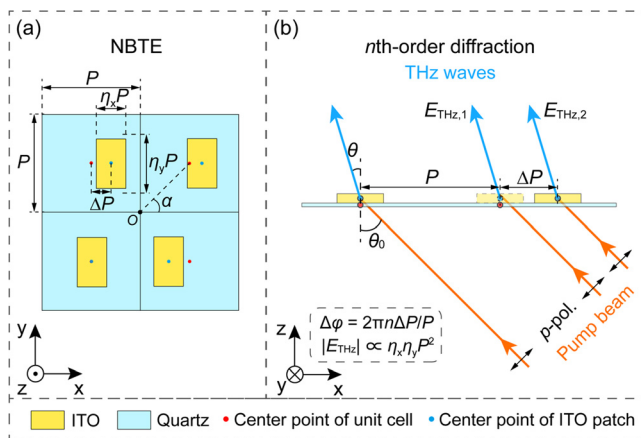

FIG. 1. Design concept of the NBTE. (a) Geometry of the unit cells. (b) Schematic of the nth-order diffraction of the THz emission from the NBTE under oblique illumination of p-polarized infrared pump beam.

$$\Delta\varphi = 2\pi\Delta P\left[\sin(\theta_0) - \sin(\theta)\right]/\lambda_{THz} = 2\pi n\Delta P/P. \quad (1)$$

This phase is well-known as the detour phase.[22,23] Clearly, $\Delta\varphi$ can cover the whole 2π range as ΔP varies between $-P/2n$ and $P/2n$ for $n \neq 0$. Moreover, the amplitude of the THz wave $|E_{THz}|$ is straightforwardly proportional to the area of the ITO patch $\eta_x\eta_y P^2$, which can cover the whole 0 to 1 range as $\eta_x (\eta_y)$ varies between 0 and 1. As a result, the phase and amplitude of the emitted THz wave at the nth-order diffraction can be simultaneously and independently controlled by, respectively, adjusting ΔP and $\eta_x\eta_y$ (η_x is kept constant here). This signifies that one can construct any THz amplitude and phase distribution on the surface of NBTE for arbitrary wavefront control in the nth-order diffraction channel.

To validate the aforementioned design concept, two kinds of NBTEs are demonstrated, with one based on sole phase control (PC), while the other on simultaneous phase and amplitude control (PAC), denoted as PC-NBTE and PAC-NBTE, respectively. Both of them are designed to work at the +1st-order diffraction ($n = +1$) for proof-of-concept demonstration, as its diffraction intensity is higher than those of the higher-order diffractions. Notice that, our method is also applicable to the higher-order diffractions. For the PC-NBTE, two functionalities are presented, including focusing beam generation and focusing vortex beam generation. In the case of focusing beam generation, the required phase distribution is only a focusing phase distribution, whereas in the case of focusing vortex beam generation, the required phase distribution becomes the summation of a focusing phase distribution and a vortex phase distribution. This operation is like placing a focusing lens and a vortex phase plate together in space. To achieve the required phase distributions, the corresponding center displacements of the ITO patches of both functionalities can be expressed as

$$\Delta P(x_u, y_u) = \frac{P}{2\pi}\Delta\varphi(x_u, y_u)$$
$$= \frac{P}{2\pi}\left[k_{THz}\left(f - \sqrt{x_u^2 + y_u^2 + f^2}\right) + \alpha(x_u, y_u)l\right] \quad (2)$$

according to Eq. (1), where (x_u, y_u) represents the coordinates of the center of the unit cell, f is the focal length, and l is the topological charge. When $l = 0$, Eq. (2) performs a beam focusing functionality; otherwise, it performs a focused vortex generation functionality. In this case, $\eta_x = 0.5$ and $\eta_y = 1$ are set for all the ITO patches to make a homogeneous amplitude distribution. For the PAC-NBTE, two devices with similar functionality are presented, which can directly emit two mixed focusing vortex beams along the same direction with different OAMs. To generate the mixed vortex beam, the required phase and amplitude distributions should be the superposition result of two different vortex fields, which can be referred to the holographic principle. Then, the focusing feature can be added by further summing up a focusing phase distribution. According to the aforementioned phase and amplitude control mechanisms, the corresponding center displacements and area sizes of the ITO patches to achieve the required phase and amplitude distributions can be expressed as

$$\begin{cases} \Delta P(x_u, y_u) = \frac{P}{2\pi}\left[k_{THz}\left(f - \sqrt{x_u^2 + y_u^2 + f^2}\right) \right. \\ \left. \qquad\qquad + \arg\left(e^{il_m\alpha(x_u,y_u)} + e^{il_n\alpha(x_u,y_u)}\right)\right], \\ \eta_x = 0.5 \text{ and } \eta_y(x_u, y_u) = \frac{|e^{il_m\alpha(x_u,y_u)} + e^{il_n\alpha(x_u,y_u)}|}{2}, \end{cases} \quad (3)$$
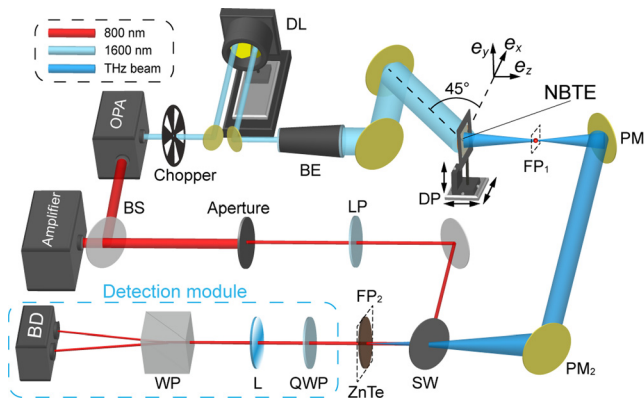
FIG. 2. Schematic of the experimental setup. OPA: optical parameter amplifier; BS: beam splitter; DL: delay line; BE: beam expander; DP: displacement platform; PM: parabolic mirror; FP_1: front focal plane of PM_1; FP_2: back focal plane of PM_2; LP: linear polarizer; SW: silicon wafer; QWP: quarter-wave plate; L: lens; WP: Wollaston prism; BD: balanced detector.

where l_m and l_n represent the topological charges of the two vortex beams.

As we mentioned earlier, THz vortex beams are promising in high-capacity communication. By adding focusing functionality, it is able to control their propagation divergence. Beyond the THz framework, focusing vortex beams are also promising in high-resolution imaging, benefitting from their beyond-diffraction-limit hollow

feature.[8,24] As for the mixed focusing vortex beams, it has been demonstrated that they can be applied in highly sensitive refractive index detection and optical tweezers.[25,26] Furthermore, the focusing functionality can also induce a higher power density and a smaller spot size at the focus region, thereby enhancing their interaction with the matters being tested as well as bringing about a higher signal-to-noise ratio and a smaller scanning area in measurement. Here, all NBTEs are fabricated on a 1-mm-thickness quartz substrate by carrying UV lithography, e-beam evaporation, and annealing process onto a 50-nm-thickness ITO film.[19] The period of the unit cell P and the focal length f of all NBTEs are configured as $425\,\mu m$ and 25 mm, respectively. Additionally, θ_0 is set to 45°, at which the THz generation efficiency of the ITO film is almost the strongest,[19] and the corresponding optical path is also easier to construct. When $\lambda_{THz} = 300\,\mu m$, the corresponding output angle of the +1st-order diffraction is at $\theta \approx 0°$.

The fabricated NBTEs are experimentally characterized using our home-made experimental setup,[19] as shown in Fig. 2. The light source is a Ti:sapphire amplifier (Legend Elite Duo, Coherent, Inc.), which emits laser pulses of 1-kHz repetition rate, 35-fs pulse duration, and 800-nm central wavelength. It is split by a BS into a reflection beam and a transmission beam. The reflection beam is applied to drive an OPA (OperA Solo, Coherent, Inc.) to generate an x-polarized infrared femtosecond laser beam whose central wavelength is tuned to 1600 nm. After passing through a chopper, a DL, and a BE in sequence, it illuminates onto the sample with an incident angle of 45° using two mirrors. The beam has a 20-mm diameter, which completely covers the NBTEs with a pump fluence of 76.4 $\mu J\,cm^{-2}$. The emitted THz beam is first collected by a 4-f system composed of PM_1 and
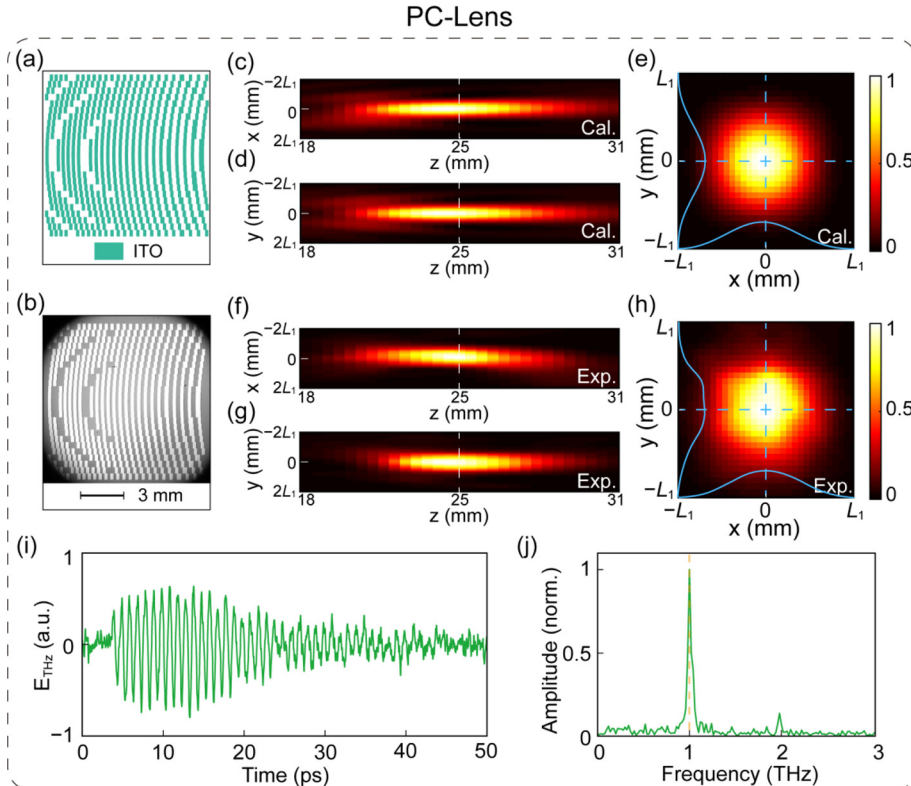
FIG. 3. Schematic and characterization of the PC-Lens. (a) and (b) Schematic and photograph of the designed PC-Lens. (c)–(h) Calculated and measured THz intensity distributions in the x-z section, y-z section, and x-y section around the focal point of the PC-Lens at 1 THz. The inset coordinate $L_1 = 0.75$ mm. The calculated and measured results are normalized by their respective common maxima. (i) and (j) Measured time-domain THz signal and corresponding normalized Fourier-transformed spectrum at the focal point of the PC-Lens, i.e., the central point of (h).
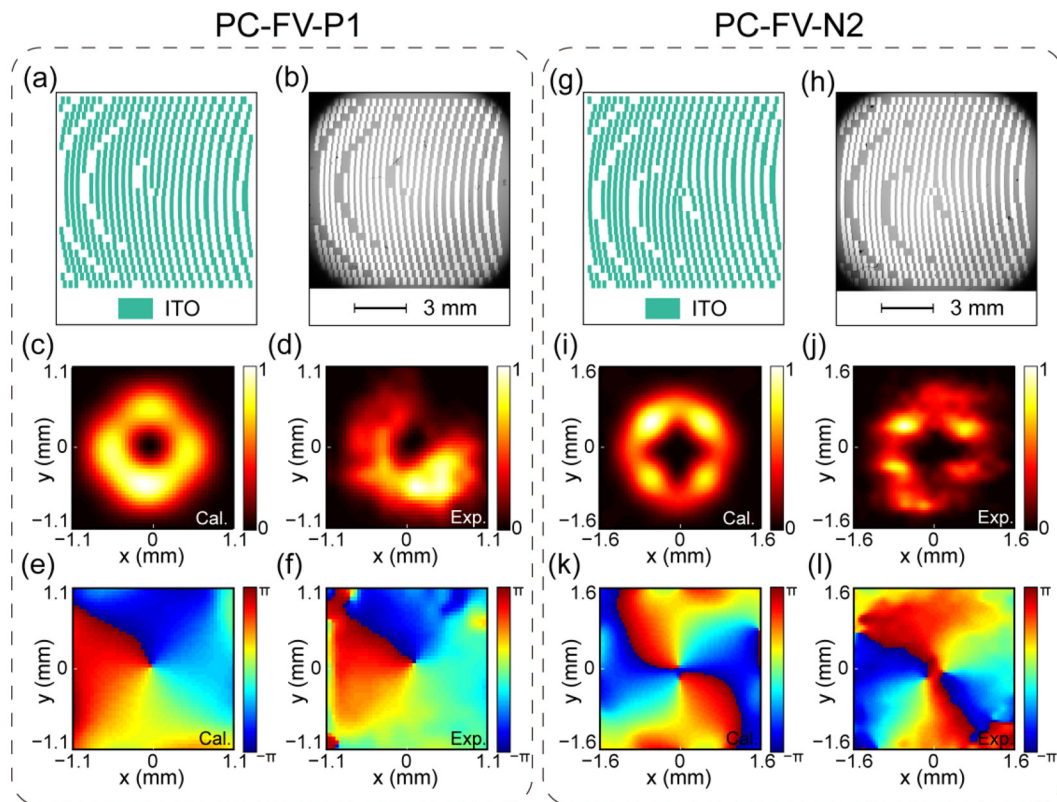
FIG. 4. Schematic and characterization of the PC-FV-P1 and the PC-FV-N2. (a), (b), (g), and (h) Schematics and photographs of the designed PC-FV-P1 and PC-FV-N2. (c)–(f) and (i)–(l) Calculated and measured THz intensity and phase distributions of the PC-FV-P1 and PC-FV-N2 in the x–y section around the focal point at 1 THz.

PM$_2$, then passes through a 2-mm-thickness polished SW, and finally illuminates on an 1-mm-thickness, $\langle 110 \rangle$-cut ZnTe crystal located at FP$_2$ for detection. As for the probe beam, it is first constrained to about 200 μm in diameter by an aperture and then horizontally polarized by an LP. After being reflected by the SW, it illuminates onto the same ZnTe crystal, aligning collinearly with the THz beam. Then, the polarization of the probe beam is modulated by the instantaneous THz electric field according to the Pockels effect. The THz field can be extracted by measuring such polarization change, which is performed by a detection model using balance detection technique. The entire THz time-domain signal is measured through stepwise moving the DL. Notice that, due to the imaging relationship of the 4-f system, only the THz signal at the focal point of PM$_1$ (red point) can be detected. Therefore, by three-dimensionally moving the NBTE positions, the spatial THz distribution can be mapped. This is achieved by mounting the NBTE onto a three-dimensional DP. During the whole movement, the NBTE can always be covered by the infrared pumping beam.

The PC-NBTE with $l = 0$ in Eq. (2), corresponding to sole focusing functionality, is first characterized, which is denoted as PC-Lens. The corresponding design schematic and sample photograph are illustrated in Figs. 3(a) and 3(b), respectively. It has an overall size of 11×11 mm^2. The pattern exhibits a distinctive leftward protruding and curved shape, which can be attributed to the interference effect between the oblique pump condition and the focusing THz emission functionality along the normal direction. To simply confirm the THz

emission behavior of the PC-Lens, the THz intensity distributions in the x-z section, y-z section, and x-y section around the focal point at 1 THz are numerically calculated utilizing the Rayleigh–Sommerfeld diffraction theory.[27] The calculated results are illustrated in Figs. 3(c)–3(e), which clearly showcase focusing characteristics along the z direction with a focal length of 25 mm and a circular focusing spot at the x-y section. Figures 3(f)–3(h) illustrate the corresponding experimental results, which closely match the calculated results, indicating a very good focusing performance of the THz emission. By extracting the intensity profiles along the horizontal and vertical lines passing the focusing center, see the blue lines in Figs. 3(e) and 3(h), we find that the calculated (experimental) spot sizes are 670 μm (700 μm) and 660 μm (680 μm) in full width at half maximum along the horizontal and vertical directions, respectively. To further explore the properties of PC-Lens, the time-domain THz signal at the focal point is extracted, as shown in Fig. 3(i). Multiple oscillation cycles are observed, which can be attributed to the differences of the spatial distances between the ITO patches and the focal point. The interference of these oscillation cycles results in a narrow bandwidth in the Fourier-transformed spectrum, as shown in Fig. 3(j). The peak amplitude just locates at 1 THz.

Next, two PC-NBTEs with $l = +1$ (P1) and -2 (N2) in Eq. (2), corresponding to focusing vortex (FV) generation functionalities, are characterized, which are denoted as PC-FV-P1 and PC-FV-N2, respectively. Figures 4(a) and 4(g) and Figs. 4(b) and 4(h) illustrate their design schematics and sample photographs, respectively. The patterns
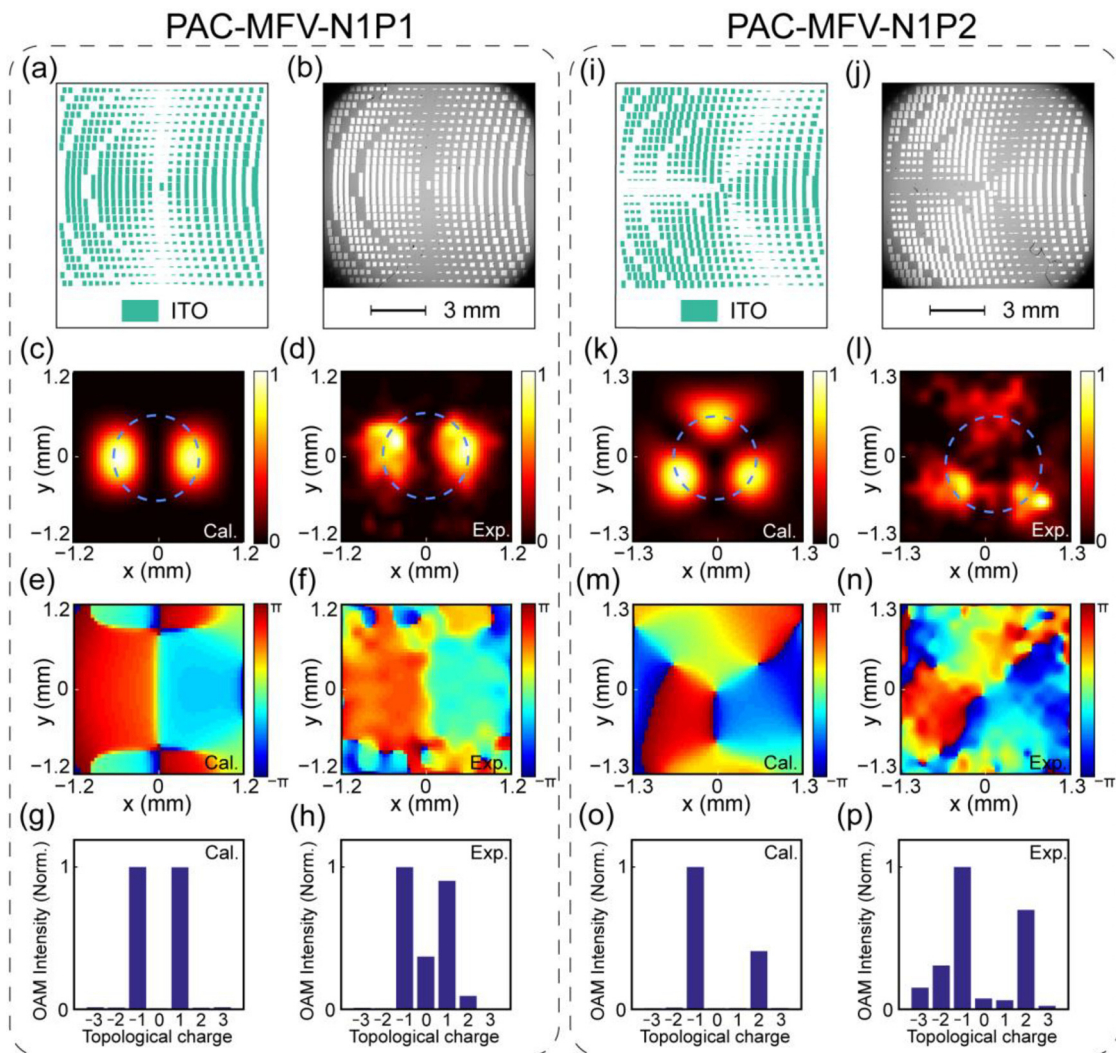
FIG. 5. Schematic and characterization of the PAC-MFV-N1P1 and the PAC-MFV-N1P2. (a), (b), (i), and (j) Schematics and photographs of the designed PAC-MFV-N1P1 and PAC-MFV-N1P2. (c)–(f) and (k)–(n) Calculated and measured THz intensity and phase distributions in the x–y section around the focal point at 1 THz. (g), (h), (o), and (p) OAM intensity distributions as a function of topological charges extracted along the blue dashed circle in (c), (d), (k), and (l), respectively.

are in the shapes of curved fork grating, which can be attributed to the interference effect of the oblique incidence condition and the focusing vortex THz emission functionalities in the design. Specifically, different signs of topological charges give opposite orientations of the fork grating along the vertical direction. The calculated and measured THz intensity and phase distributions in the x-y section around the focal point at 1 THz are shown in Figs. 4(c)–4(f) for PC-FV-P1 and Figs. 4(i)–4(l) for PC-FV-N2, respectively. Both THz intensity distributions display hollow ring patterns, while the phase distributions exhibit a 2π and a -4π variations along the azimuthal direction, which are clear features of a +1st-order and a −2nd-order vortex THz beams. The size of the +1st-order THz vortex beam is smaller than that of the −2nd-order THz vortex beam, since the higher-order vortex beam has a larger divergence angle. The inhomogeneity of the calculated

intensity distributions can be ascribed to the limited aperture size of our designed NBTEs. The measured results are well consistent with the calculated results. The slight mismatch can be attributed to the inhomogeneity of the fabricated ITO, which causes inhomogeneous THz emission amplitudes as well as the fluctuation of the experimental setup. All the aforementioned evidences well verify our phase control method. To show the advantage of the proposed phase control method as compared to the previous 1-bit phase control method in building PC-NBTEs, numerical calculations are carried out (see supplementary material Note 1). It is found that the intensities of all the generated THz beams by the proposed method are much stronger than those by 1-bit method, even though they exhibit nearly the same intensity and phase patterns. This can be attributed to the fact that the proposed phase control is arbitrary, which can make the emitted THz wave from

30 April 2024 02:04:34

each ITO patch constructively interfere with each other around the focal point very well, while the 1-bit phase control cannot, owing to its limited phase resolution.

Finally, the PAC-NBTEs with $l_{\mathrm{m}} = -1$, $l_{\mathrm{n}} = +1$ (N1P1) and $l_{\mathrm{m}} = -1$, $l_{\mathrm{n}} = +2$ (N1P2) in Eq. (3), corresponding to mixed focusing vortex (MFV) beam generation functionalities, are characterized, which are denoted as PAC-MFV-N1P1 and PAC-MFV-N1P2, respectively. Figures 5(a) and 5(i) and Figs. 5(b) and 5(j) illustrate their design schematics and sample photographs, respectively. The overall patterns of PAC-MFV-N1P1 and PAC-MFV-N1P2 are split into two and three parts, which can be ascribed to the change of η_y caused by vortex interference in Eq. (3). The calculated and measured THz intensity and phase distributions in the x-y section around the focal point at 1 THz are shown in Figs. 5(c)–5(f) for PAC-MFV-N1P1 and Figs. 5(k)–5(n) for PAC-MFV-N1P2. Two and three sidelobes for PAC-MFV-N1P1 and PAC-MFV-N1P2 are observed in the THz intensity distributions, while the corresponding phase distributions show two and three main phase areas, respectively, which are all clear evidence of the designed vortex interference. In addition, the OAM intensity distributions as a function of topological charges are extracted along the blue dashed circle in Figs. 5(c), 5(d), 5(k), and 5(l), as shown in Figs. 5(g), 5(h), 5(o), and 5(p), respectively. It can be seen that the OAM intensities for the PAC-MFV-N1P1 (PAC-MFV-N1P2) at the topological charges of -1 and $+1$ (-1 and $+2$) are remarkably higher than others, which agrees well with the design. The measured results again agree well with the calculated results. The undesired noise in the measured results and the crosstalk OAM intensities at the other topological charges can be ascribed to the inhomogeneity of fabricated ITO, and the limited signal sensitivity and stability of our experimental setup. Nonetheless, the simultaneous phase and amplitude control ability of our method is well verified.

In summary, we have demonstrated a generic method for manipulating the wavefronts of diffracted THz emission using patterned ITO films under an infrared femtosecond laser pump. This method allows for fully local manipulation of both phase and amplitude of the emitted THz wave along the +1st-order diffraction, which is achieved by simultaneously controlling the displacement and area of the ITO patch within each unit cell. This enables various wavefront control functionalities, including focusing, single focusing vortex, and mixed focusing vortex THz emissions. Nevertheless, this method can, in principle, be extended to design arbitrary wavefronts of THz emission along any allowed diffraction order at any THz frequency under oblique pump. It is important to note that our method is not limited to ITO films and can be applied to any kind of nonlinear material, such as spintronic film[18] and graphene.[28] This universality further enhances the potential of our work in paving the way for miniaturized, functional, and cost-effective THz emission and manipulation technology. The implications of our research are particularly promising for high-speed communication and imaging applications in the future. With further development and optimization, our method could promote THz technology and enable a wide range of practical applications.

See the supplementary material for comparison between PC-NBTEs with arbitrary phase control and 1-bit phase control.

AUTHOR DECLARATIONS
Conflict of Interest

The authors have no conflicts to disclose.

Author Contributions

Xi Feng: Conceptualization (lead); Formal analysis (equal); Methodology (lead); Software (lead); Writing – original draft (lead); Writing – review & editing (supporting). **Xueqian Zhang:** Formal analysis (equal); Funding acquisition (equal); Supervision (equal); Writing – review & editing (equal). **Haidi Qiu:** Resources (equal). **Quan Xu:** Formal analysis (equal); Funding acquisition (equal); Supervision (equal); Writing – review & editing (equal). **Weili Zhang:** Funding acquisition (equal); Project administration (equal); Supervision (equal). **Jiaguang Han:** Funding acquisition (equal); Project administration (equal); Supervision (equal); Writing – review & editing (equal).

DATA AVAILABILITY

The data that support the findings of this study are available from the corresponding authors upon reasonable request.

REFERENCES

[1] T. Nagatsuma, G. Ducournau, and C. C. Renaud, Nat. Photonics **10**, 371 (2016).

[2] S. Ding, J.-Y. Ou, L. Du, L. Zhu, S. A. Khan, H. Chen, and J. Zhu, Carbon **179**, 666 (2021).

[3] W. Xu, L. Xie, and Y. Ying, Nanoscale **9**, 13864 (2017).

[4] Y. Cheng, L. Qiao, D. Zhu, Y. Wang, and Z. Zhao, Opt. Lett. **46**, 1233 (2021).

[5] Q. Wang, X. Zhang, Y. Xu, Z. Tian, J. Gu, W. Yue, S. Zhang, J. Han, and W. Zhang, Adv. Opt. Mater. **3**, 779 (2015).

[6] H. Zhao, B. Quan, X. Wang, C. Gu, J. Li, and Y. Zhang, ACS Photonics **5**, 1726 (2018).

[7] X. Zang, B. Yao, L. Chen, J. Xie, X. Guo, A. V. Balakin, A. P. Shkurinov, and S. Zhuang, Light: Adv. Manuf. **2**, 10 (2021).

[8] H. Wang, Q. Song, Y. Cai, Q. Lin, X. Lu, H. Shangguan, Y. Ai, and S. Xu, Chin. Phys. B **29**, 097404 (2020).

[9] K. Miyamoto, B. J. Kang, W. T. Kim, Y. Sasaki, H. Niinomi, K. Suizu, F. Rotermund, and T. Omatsu, Sci. Rep. **6**, 38880 (2016).

[10] A. A. Ushakov, P. A. Chizhov, V. V. Bukin, and S. V. Garnov, Bull. Lebedev Phys. Inst. **46**, 336 (2019).

[11] T. Wu, Q. Xu, X. Zhang, Y. Xu, X. Chen, X. Feng, L. Niu, F. Huang, J. Han, and W. Zhang, Adv. Sci. **9**, 2204664 (2022).

[12] T. Wu, X. Zhang, Q. Xu, E. Plum, K. Chen, Y. Xu, Y. Lu, H. Zhang, Z. Zhang, X. Chen, G. Ren, L. Niu, Z. Tian, J. Han, and W. Zhang, Adv. Opt. Mater. **10**, 2101223 (2022).

[13] Q. Lin, S. Zheng, Q. Song, X. Zeng, Y. Cai, Y. Li, Z. Chen, L. Zha, X. Pan, and S. Xu, Opt. Lett. **44**, 887 (2019).

[14] K. Miyamoto, K. Sano, T. Miyakawa, H. Niinomi, K. Toyoda, A. Valles, and T. Omatsu, Opt. Express **27**, 31840 (2019).

[15] E. Minerbi, S. Keren-Zur, and T. Ellenbogen, Nano Lett. **19**, 6072 (2019).

[16] Y. Lu, X. Feng, Q. Wang, X. Zhang, M. Fang, W. E. I. Sha, Z. Huang, Q. Xu, L. Niu, X. Chen, C. Ouyang, Y. Yang, X. Zhang, E. Plum, S. Zhang, J. Han, and W. Zhang, Nano Lett. **21**, 7699 (2021).

[17] Q. Wang, X. Zhang, Q. Xu, X. Feng, Y. Lu, L. Niu, X. Chen, E. Plum, J. Gu, Q. Yang, M. Fang, Z. Huang, S. Zhang, J. Han, and W. Zhang, Adv. Funct. Mater. **33**, 2300639 (2023).

[18] S. Chen, H. Wang, J. Liu, M. Zhang, P. Chen, P. Li, Z. Liu, X. Han, C. Wan, H. Yu, Y. Zhang, and X. Wu, Adv. Opt. Mater. **12**, 2300899 (2024).

[19]X. Feng, X. Chen, Y. Lu, Q. Wang, L. Niu, Q. Xu, X. Zhang, J. Han, and W. Zhang, Adv. Opt. Mater. **11**, 2201628 (2023).

[20]W. Jia, M. Liu, Y. Lu, X. Feng, Q. Wang, X. Zhang, Y. Ni, F. Hu, M. Gong, X. Xu, Y. Huang, W. Zhang, Y. Yang, and J. Han, Light: Sci. Appl. **10**, 11 (2021).

[21]Y. Lu, X. Zhang, Q. Xu, W. Jia, X. Feng, X. Chen, Y. Gu, Y. Yang, W. Zhang, and J. Han, ACS Photonics **11**, 293 (2024).

[22]M. Khorasaninejad, A. Ambrosio, P. Kanhaiya, and F. Capasso, Sci. Adv. **2**, e1501258 (2016).

[23]Z. L. Deng, M. Jin, X. Ye, S. Wang, T. Shi, J. Deng, N. Mao, Y. Cao, B. O. Guan, A. Alù, G. Li, and X. Li, Adv. Funct. Mater. **30**, 1910610 (2020).

[24]C. Jansen, S. Wietzke, O. Peters, M. Scheller, N. Vieweg, M. Salhi, N. Krumbholz, C. Jördens, T. Hochrein, and M. Koch, Appl. Opt. **49**, E48 (2010).

[25]A. H. Dorrah, M. Zamboni-Rached, and M. Mojahedi, Light: Sci. Appl. **7**, 40 (2018).

[26]G. Liang, B. Yuan, Y. Li, X. Kong, W. Cheng, H. Qiao, and X. Hu, Results Phys. **26**, 104352 (2021).

[27]Q. Wang, X. Zhang, Y. Xu, J. Gu, Y. Li, Z. Tian, R. Singh, S. Zhang, J. Han, and W. Zhang, Sci. Rep. **6**, 32867 (2016).

[28]J. Maysonnave, S. Huppert, F. Wang, S. Maero, C. Berger, W. de Heer, T. B. Norris, L. A. De Vaulchier, S. Dhillon, J. Tignon, R. Ferreira, and J. Mangeney, Nano Lett. **14**, 5797 (2014).

30 April 2024 02:04:34